ENHANCED AVIONIC SENSING BASED ON WIGNER'S CUSP ANOMALIES

Joshua Feinberg

University of Haifa

Analytic and Algebraic Methods in Physics
XIX
Czech Technical University, Prague
9 September 2022

Work done in collaboration with
Rodion Kononchuk, Joseph Knee & Tsampikos Kottos

based on: Science Advances 7(2021) eabg8118

Motivation

Avionic sensing?

(not to worry - this is not an engineering talk)

Airplane navigation systems employ precise accelerometers.

The accelerometer measures the instantaneous acceleration of the airplane and feeds it to the flight computer.

The computer then integrates the equations of motion to find the instantaneous location of the airplane in space.

Other uses of high-sensitivity accelerometers:

- navigation
- gravity radiometry
- earthquake monitoring
- platform stabilization for space applications
- home security (intruder detection)
- airbag deployment in cars
- more ….

Typical accelerometers

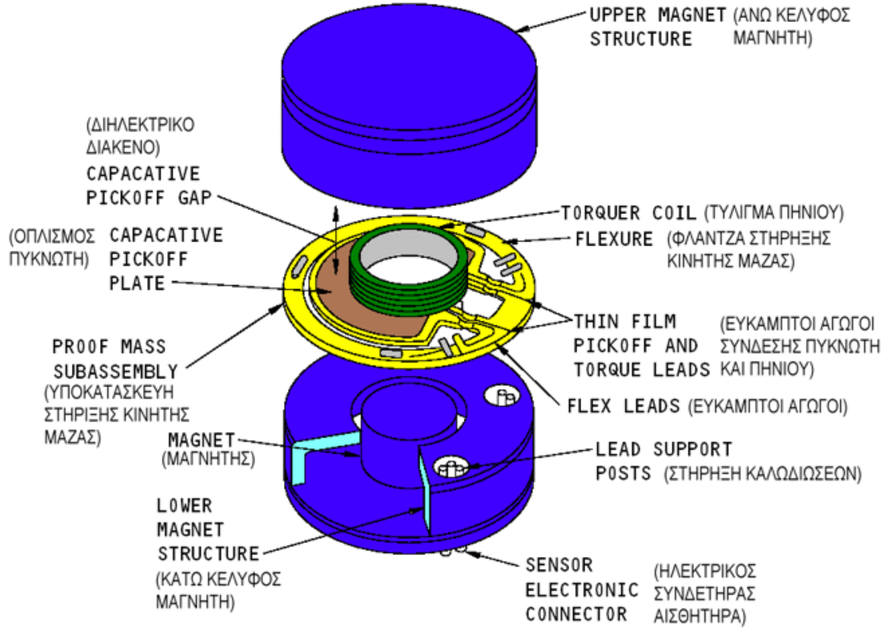

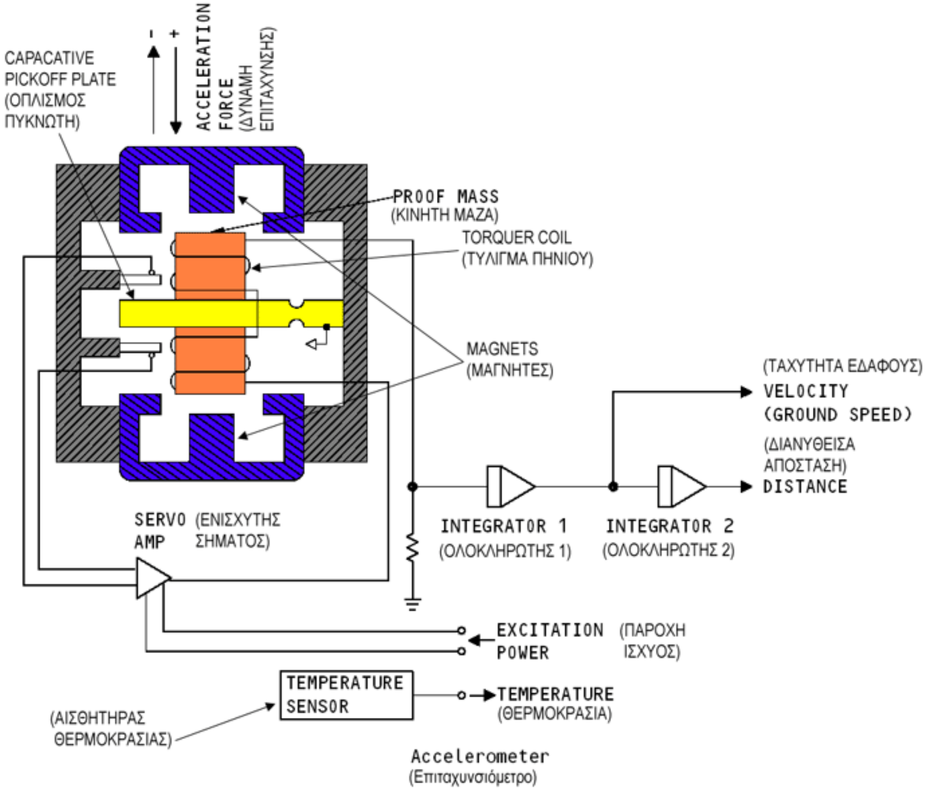

https://www.k-makris.gr/accelerometer/

Kostas Makris, a Licensed Aircraft Engineer

Typically, accelerometers use **linear sensors**: the output is (ultimately an electronic) signal proportional to the instantaneous acceleration.

the sensor detects the displacement of a test mass

$$\text{output (electric signal)} = C \times \text{input (acceleration)}$$

$$\text{sensitivity} = d(\text{output})/d(\text{input}) = C$$

fixed sensitivity C

want to make C as large as possible, which is naturally ***limited***

Developing detectors that go beyond linear response might lead to marked enhancement of small-acceleration sensing, without sacrificing the dynamical range of the sensor

dynamical range of the sensor = ratio between the maximal and minimal acceleration measurable by the sensor

a prominent example of such detectors: resonant systems near N-th order exceptional point degeneracy:

a small perturbation ~ $\epsilon \ll 1$ activates sub-linear response ~ $\epsilon^{1/N} \gg \epsilon$

in resonance splitting

J. Wiersig, Enhancing the sensitivity of frequency and energy splitting detection by using exceptional points: Application to microcavity sensors for single-particle detection. *Phys. Rev. Lett.* **112**, 203901 (2014).

J. Wiersig, Prospects and fundamental limits in exceptional point-based sensing. *Nat. Comm.* **11**, 2454 (2020).

L. Feng, R. El-Ganainy, L. Ge, Non-Hermitian photonics based on parity-time symmetry. *Nat. Photonics* **11**, 752–762 (2017).

M. Parto, Y. G. N. Liu, B. Bahari, M. Khajavikhan, D. N. Christodoulides, Non-Hermitian and topological photonics: Optics at an exceptional point. *Nanophotonics* **10**, 403 (2021).

implementation by using micro resonators

H. Hodaei, A. U. Hassan, S. Wittek, H. Garcia-Gracia, R. El-Ganainy, D. N. Christodoulides, M. Khajavikhan, Enhanced sensitivity at higher-order exceptional points. *Nature* **548**, 187–191 (2017).
W. Chen, S. K. Ozdemir, G. Zhao, J. Wiersig, L. Yang, Exceptional points enhance sensing in an optical microcavity. *Nature* **548**, 192–196 (2017).

in avionic gyroscopes

M. P. Hokmabadi, A. Schumer, D. N. Christodoulides, M. Khajavikhan, Non-Hermitian ring laser gyroscopes with enhanced Sagnac sensitivity. *Nature* **576**, 70–74 (2019).
Y.-H. Lai, Y.-K. Lu, M.-G. Suh, Z. Yuan, K. Vahala, Observation of the exceptional-point-enhanced Sagnac effect. *Nature* **576**, 65–69 (2019).

these gyros are formed by judiciously distributing gain between interacting modes of a photonic cavity, often leading to excessive quantum noise, that might inhibit the enhanced sensing

J. Wiersig, Prospects and fundamental limits in exceptional point-based sensing. *Nat. Comm.* **11**, 2454 (2020).

Y.-H. Lai, Y.-K. Lu, M.-G. Suh, Z. Yuan, K. Vahala, Observation of the exceptional-point-enhanced Sagnac effect. *Nature* **576**, 65–69 (2019).
H. Wang, Y.-H. Lai, Z. Yuan, M.-G. Suh, K. Vahala, Petermann-factor sensitivity limit near an exceptional point in a Brillouin ring laser gyroscope. *Nat. Comm.* **11**, 1610 (2020).

our proposal: accelerator with enhanced sensing capability based on sub-linear variations of scattering cross-sections to small perturbations.

sub-linear response occurs due to ***Wigner's cusp anomaly*** (WCA) of the cross-section at threshold between an open and closed scattering channel

then use the sub-linear Puiseux expansion for the reflectance/transmittance near threshold for hypersensing

The advantage of our proposal over the exceptional-point based gyros: our WCA protocol is based on intensity measurements (transmittance/reflectance) and not on resonant shift. The latter is sometimes masked by broadening of the transmission (or reflection) spectrum, and also in the presence of gain elements, by the unavoidable addition of quantum noise.

We thus propose WCA-based sensors as simple, yet hypersensitive devices for a variety of applications ranging from avionics to bio- and chemical sensing.

fundamental principle behind WCA (L&L vol 3)

(I shall explain it for NRQM, but this holds also to many phenomena of wave propagation, in particular, of EM waves)

scattering cross section from an initial channel i to final channel f: $d\sigma_{fi} = |f_{fi}|^2 \frac{p_f}{p_i} d\Omega_f$

assume time-reversal invariance T $f_{fi} = f_{i*f*}$ (reciprocity)

inverts signs of all momenta (and spins)

$$d\sigma_{i*f*} = |f_{i*f*}|^2 \frac{p_i}{p_f} d\Omega_i$$

$$|f_{fi}|^2 = |f_{i*f*}|^2 \Rightarrow \quad \frac{1}{p_f^2}\frac{d\sigma_{fi}}{d\Omega_f} = \frac{1}{p_i^2}\frac{d\sigma_{i*f*}}{d\Omega_i}$$ (detailed balance)

at threshold for i —> f $\qquad p_f \sim \sqrt{\epsilon} \ll 1$

incident flux for threshold for f* —> i* $\qquad v_f \sim p_f \sim \sqrt{\epsilon}$

f_{i*f*} finite at threshold $\quad \Rightarrow \frac{d\sigma_{i*f*}}{d\Omega_i}|_{threshold} \sim \frac{1}{v_f} \sim \frac{1}{\sqrt{\epsilon}}$

$$\frac{1}{p_f^2}\frac{d\sigma_{fi}}{d\Omega_f} = \frac{1}{p_i^2}\frac{d\sigma_{i*f*}}{d\Omega_i} \qquad \Rightarrow \frac{d\sigma_{fi}}{d\Omega_f} \sim \frac{p_f^2}{p_f p_i^2} \sim \sqrt{\epsilon}$$

In simple terms, the near threshold behavior $\frac{d\sigma_{fi}}{d\Omega_f} \sim v_f \sim \sqrt{\epsilon}$

demonstrates the well-known fact that in a scattering process between propagating modes carrying currents

J_i, J_f the transmittance is $T_{f,i,} \sim \frac{J_f}{J_i} \sim \frac{v_f}{v_i} \sim \sqrt{\epsilon}$

From L&L v3, single channel threshold

$$\sigma = \sigma_t - 2A\sqrt{(|E-E_t|)} \times \begin{cases} \sin^2 \delta_0 & \text{for } E > E_t, \\ \sin \delta_0 \cos \delta_0 & \text{for } E < E_t. \end{cases}$$

For the general case of n-channels see our paper

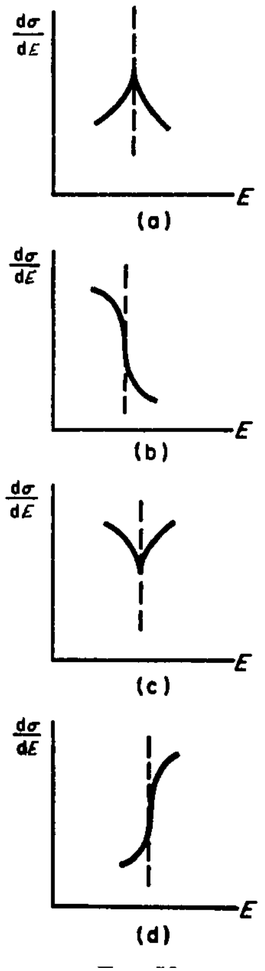

WCAs in different physical systems

The simplest example leading to WCA is one-dimensional scattering of a nonrelativistic particle by a step potential of height U extending over $x \geq 0$ (see Fig. 1B). For $x < 0$, the energy dispersion relation is $E = k_i^2$ (units of $\hbar^2/2m = 1$) where E and k_i are the incident energy and the wave vector, while for $x > 0$, we have $k_f = \sqrt{E - U}$. Threshold occurs at energy $E_t = U$, signifying a transition from a real (for $E > E_t$) to an imaginary (for $E < E_t$) wave vector k_f (corresponding to an evanescent wave). Above (below) threshold $E > U (E < U)$, the reflectance is $R = \left(\frac{k_f - k_i}{k_f + k_i}\right)^2 \approx 1 - 4\sqrt{\frac{E-U}{U}}$ $(R = 1)$, while the corresponding transmittance is $T = 4\frac{k_i k_f}{(k_f + k_i)^2} \approx 4\sqrt{\frac{E-U}{U}}$ $(T = 0)$, which nicely demonstrates the leading square-root term of the systematic Puiseux expansion of these quantities.

B

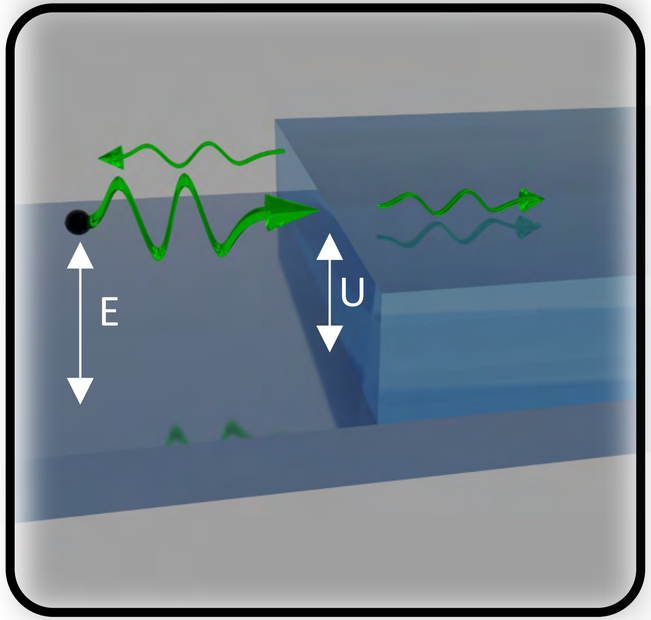

The analogous scenario in optics is associated with light scattering through a dielectric interface from a medium with high refractive index $n_i = n_H$ to a medium with a low refractive index $n_f = n_L$ (see Fig. 1C). Assuming that the direction of the normal from the boundary plane is along the z axis, the problem is rotation-invariant around this axis. Consequently, without loss of generality, the direction of propagation can be taken to lie in the xz plane. The dispersion relations on each side of the interface are $k_{i,f}^z = \sqrt{(\frac{\omega}{c} n_{i,f})^2 - (k^x)^2}$, where $\mathbf{k} = (k^x, k^y, k^z)$. Furthermore, $k^x = \frac{\omega}{c} n_i \sin\theta_i$, where θ_i is the incidence angle with respect to the normal to the interface and Snell's law guarantees continuity of k^x. Here, threshold behavior occurs at the critical angle $\theta_i = \theta_c = \arcsin(\frac{n_L}{n_H})$, corresponding to $k_f^z = 0$. The reflection r and transmission t amplitudes are given by the same expressions as in the quantum step example, with k_i and k_f substituted by $k_{i,f}^z$. Just below the critical angle $\theta = \theta_c - \varepsilon$ $(0 < \varepsilon \ll 1)$, we can expand r, t in a Puiseux series, leading to the polarization-dependent reflectance (transmittance)

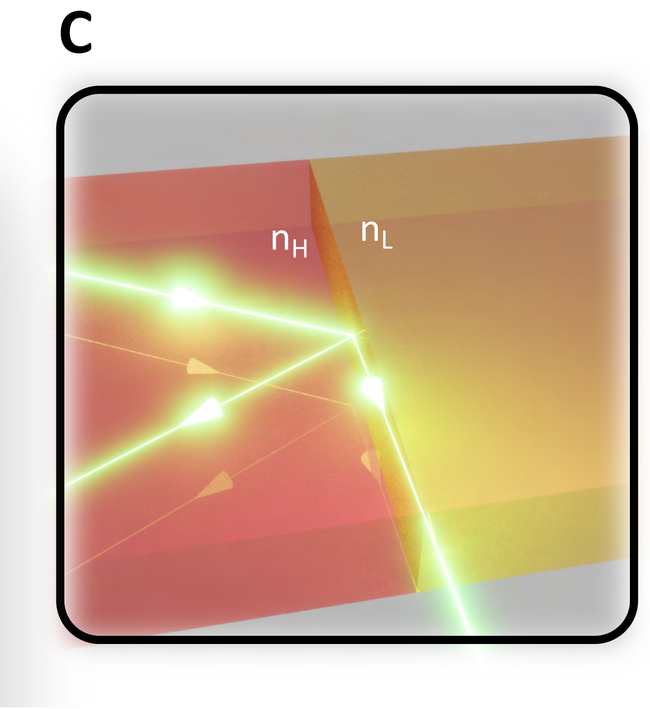

$$R \equiv |r|^2 \propto 1 - 2A_\delta\sqrt{\varepsilon}, T \equiv |t|^2 \propto 2A_\delta\sqrt{\varepsilon}$$

where $A_\delta = 2\gamma_\delta^2\sqrt{2(\tilde{n}^2 - 1)^{-\frac{1}{2}}}, \tilde{n} = n_H/n_L$ is a refractive index ratio between the two media, $\delta = p, s$ denotes the s- and p-polarized light, respectively, and $\gamma_{\delta=s} = 1$, while $\gamma_{\delta=p} = \tilde{n}\, n$. These equations show that this scattering process results in the formation of a WCA associated with the opening/closing of a scattering channel k_f^z at a critical incidence angle θ_c.

WCAs are ubiquitous and can be implemented in a variety of other photonic platforms. We can, for example, implement them in one-dimensional coupled resonators optical waveguide (CROW) arrays at the vicinity of a band edge. A simple realization is shown in Fig. 1D, where two CROW arrays with resonant detuning $0 < U < 2|t_1 + t_2|$ and coupling constants $t_{1,2} < 0$ are brought together. When the detuning U varies (e.g., due to exposure of one of the two CROWs to a biological agent or changes of the ambient temperature or illumination), the transmittance/reflectance exhibits WCA for frequencies near the band edges associated with the common transmission frequency domain (see the Supplementary Materials for detailed analysis). Another implementation of WCA involves a uniform multimode waveguide (see Fig. 1E) in the vicinity of a mode threshold. In this case, cross-sectional variations (e.g., due to pressure variations) will induce the closing/opening of a channel at one portion of the waveguide, which, in turn, will be sensed as transmittance changes following a sublinear WCA

D

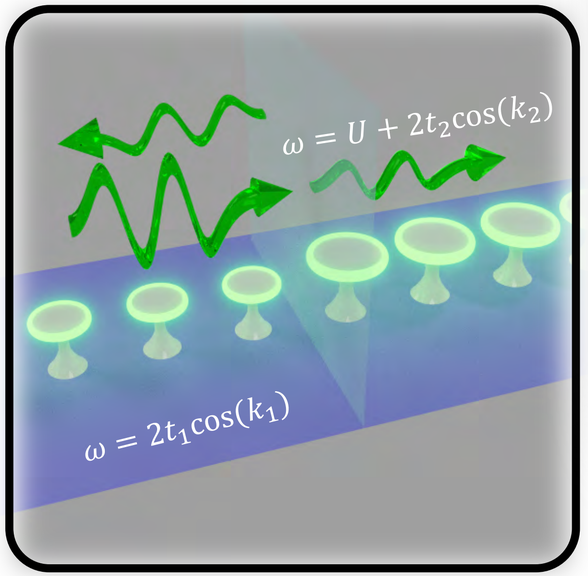

E

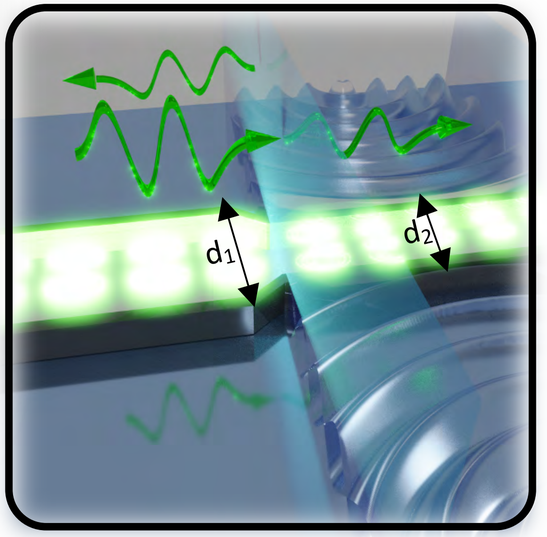

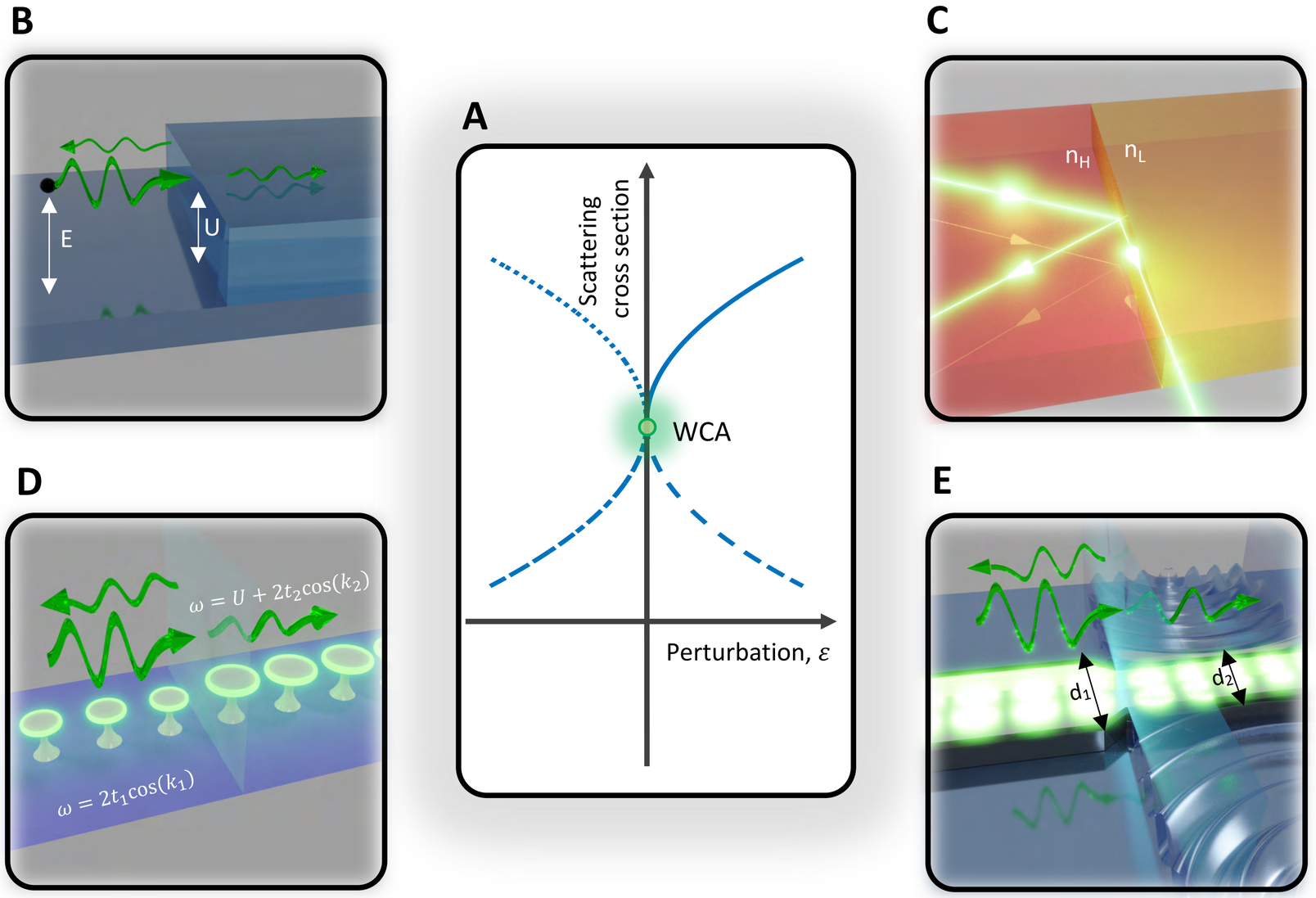

Fig. 1. Various WCA settings. (**A**) A WCA describing a square-root behavior of the scattering cross section in the vicinity of a channel threshold. Various forms of WCA are represented by different line styles (for details, see the Supplementary Materials). (**B**) Scattering of a quantum particle from a step potential of height U. (**C**) Near TIR of a monochromatic wave from the interface between two dielectric media with reflection indices $n_i = n_H > n_f = n_L$. (**D**) Two CROW transmission lines with resonant frequency detuning U. (**E**) A waveguide whose (right) portion is exposed to pressure variations leading to a distortion of its cross section, which induces a threshold WCA.

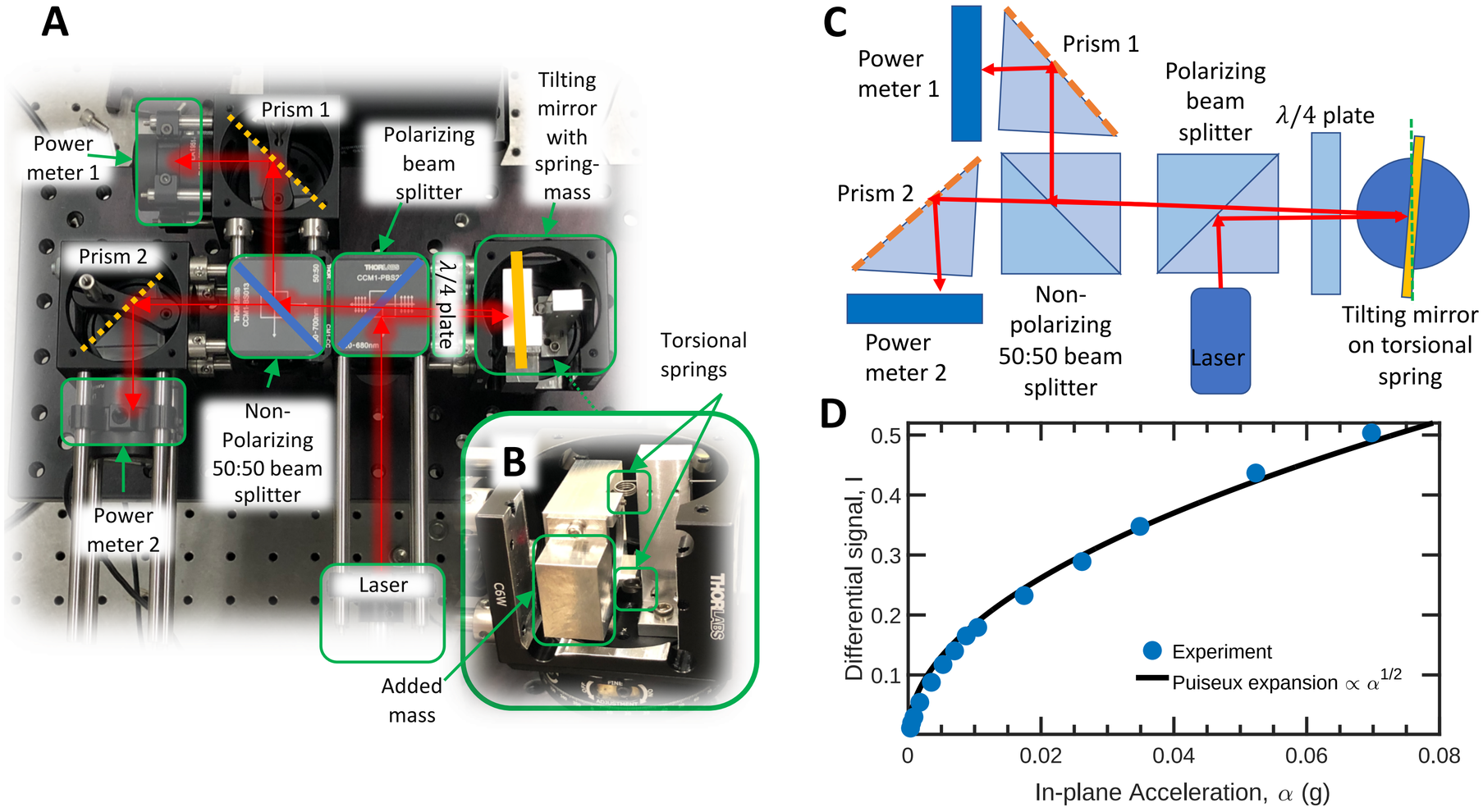

Fig. 2. WCA accelerometer. (**A**) Experimental implementation of the TIR as a WCA protocol for a hypersensitive accelerometer. (**B**) Magnification of the mirror with the attached test mass that is coupled to two torsional springs. (**C**) Schematic description of the platform shown in (A). (**D**) Measured differential signal *I* versus in-plane acceleration α (filled blue circles). The system is calibrated to demonstrate a TIR when it is at rest. Any acceleration will lead to a WCA. The black line indicates the Puiseux expansion near WCA. Photo credit: (A and B) Rodion Kononchuk, Wesleyan University.

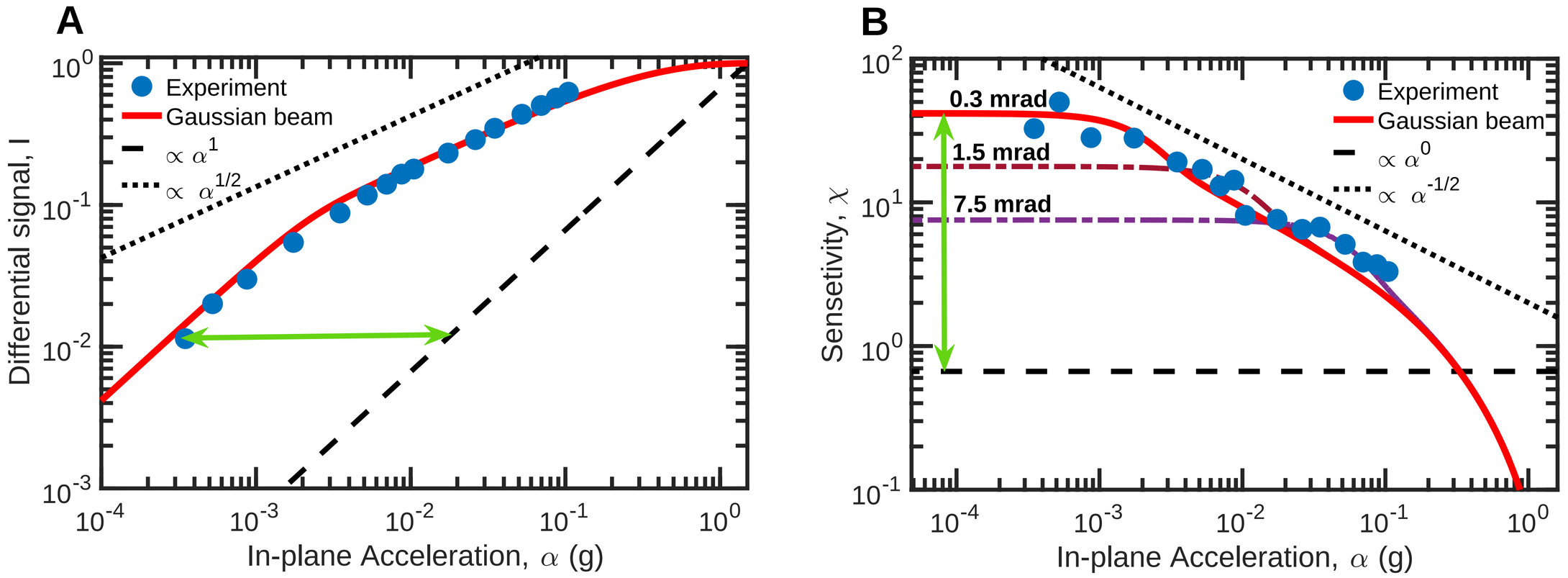

Fig. 3. Beam divergence effects and WCA-sensitivity. (**A**) Measured differential signal *I* versus in-plane accelerations α (blue filled circles) reported in log-log plot. The theoretical calculation that incorporates the Gaussian beam divergence of 0.3 mrad is shown in the red solid line. The black dotted line has a slope of $^1/_2$, while the black dashed line indicates the linear slope of the conventional acceleration sensor with the same maximum output and with linear sensitivity. The green double-sided arrow indicates the dynamic range enhancement of the proposed WCA sensor. (**B**) Measured sensitivity of the accelerometer $\chi \equiv dI/d\alpha$ (blue filled circles). The red solid line describes the theoretical curve that takes into consideration the Gaussian beam divergence associated with the characteristics of our lasing source (0.3-mrad beam divergence). In the same figure, we also report with a dark red (purple) dashed-dotted line the theoretically calculated sensitivity for a lasing source with a beam divergence of 1.5 mrad (7.5 mrad). The black dotted line has a slope of $-^1/_2$, while the black dashed line indicates a constant sensitivity $\chi = 0.67\ g^{-1}$ of a conventional linear accelerometer (see the main text). The green double-sided arrow indicates the sensitivity enhancement of the proposed WCA sensor.

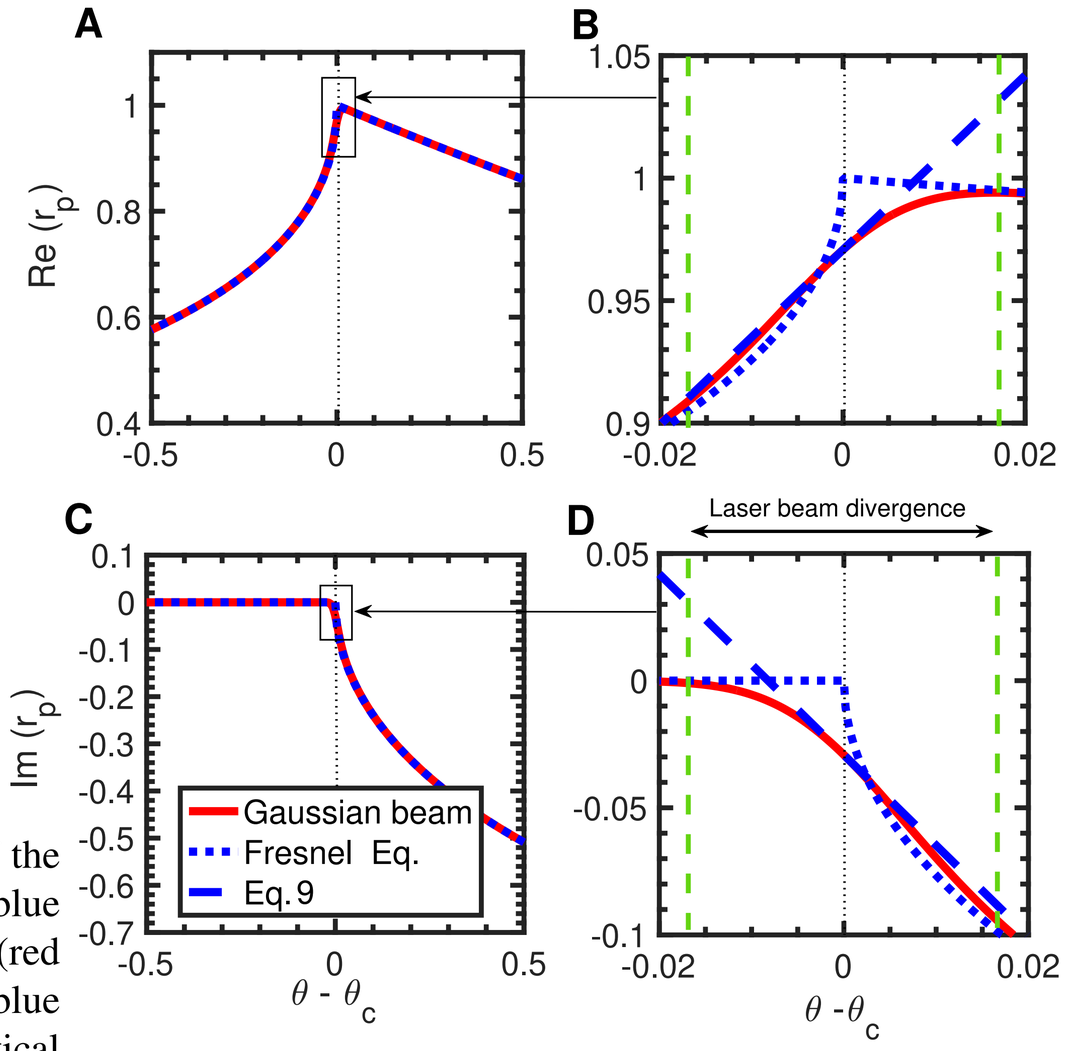

Figure S1: **Reflection of Gaussian beam from a dielectric interface**: **(A)** Real part of the reflection amplitude of the p-polarized $\mathcal{R}e(r_p)$ light calculated using Fresnel's equations (blue dotted line) and taking into consideration divergence effects due to a Gaussian beam shape (red line). **(B)** Magnification of the domain around the black square frame shown in **(A)**. The blue dashed line is the linear approximation calculated from Eq. (9) (see main text), while the vertical green dashed lines indicate the Gaussian laser beam divergence used in the calculations. **(C)** The imaginary part of the reflection amplitude of the p-polarized $\mathcal{I}m(r_p)$ light calculated using Fresnel's equations (blue dashed line) and taking into consideration the divergence effects of the Gaussian beam (red line). **(D)** Magnification of the domain around the black square frame shown in **(C)**. The blue dashed line is the linear approximation calculated from Eq (9) (see main text), while the vertical green dashed lines indicate the Gaussian laser beam divergence used in the calculations.

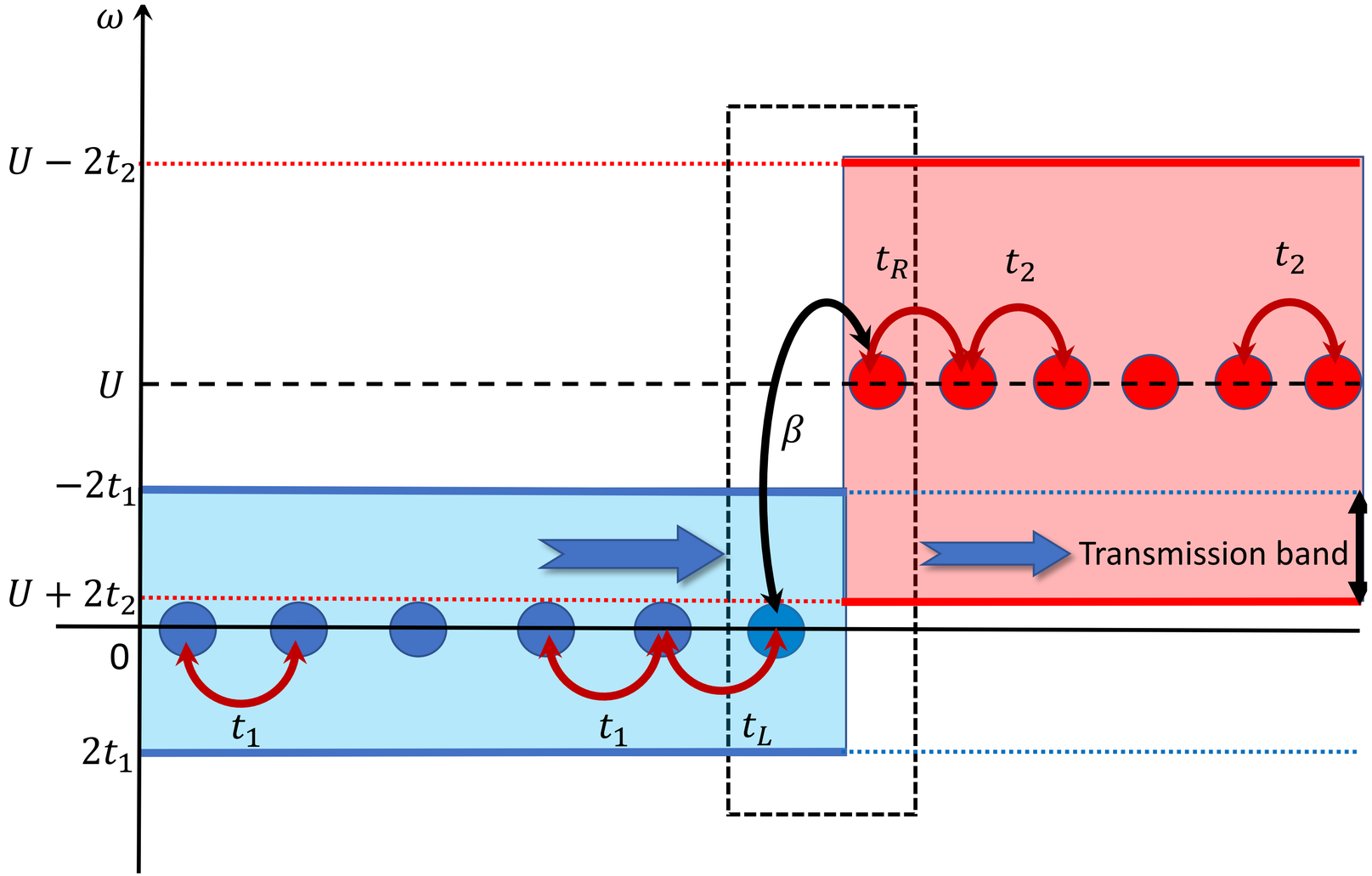

Figure S3: **Schematics of the CROW array interface**. Left/right CROW transmission lines are shown by blue/red resonators (see also Fig. 1D of the main text). The supported bands of the left/right transmission lines are shown by the blue/red region. The black vertical arrow indicates the region where the bands overlap forming a transmission band of the interface. The black dashed box indicates the system described by the Hamiltonian H_0.

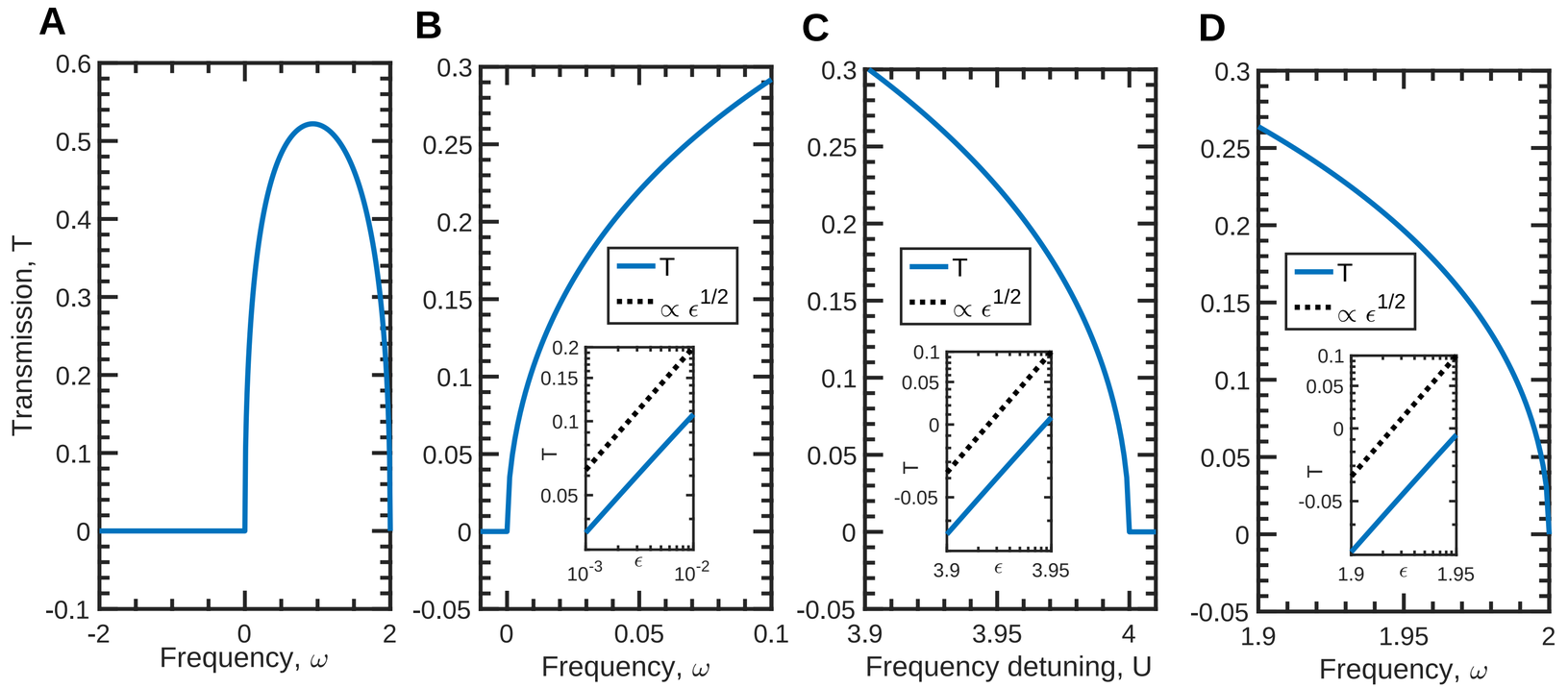

Figure S4: **Transmission Spectrum and WCA for a CROW array.** **(A)** Transmission spectrum of the CROW array interface shown in Fig. S3 (see also Fig. 1D). The parameters used are $t_1 = -1$, $t_2 = -2$, $\beta = -1$ and $U = 4$. The transmission band in this case is within the frequency range of $\omega \in [0, 2]$. **(B)** Magnification of the transmission spectrum at the vicinity of the lower frequency threshold corresponding to $\omega_t^{(1)} = 0$. In the inset we show in a log-log plot the dependence of transmittance T for small frequency detunings $\epsilon = \omega - \omega_t^{(1)}$. **(C)** Dependence of the transmittance from the CROW detuning parameter U near its threshold value $U_t = 4$ for an incident wave at fixed frequency $\omega = \omega_t^{(1)}$. In the inset we show the transmittance versus $\epsilon = U_t - U$ in log-log plot. **(D)** Transmission spectrum near the upper frequency threshold $\omega_t^{(2)} = 2$. In the inset we plot the transmittance versus detuning $\epsilon = \omega_t^{(2)} - \omega$ in a log-log plot. The black dashed lines in subfigures **(B-D)** is proportional to $\sqrt{\epsilon}$ and is drawn in order to guide the eye.

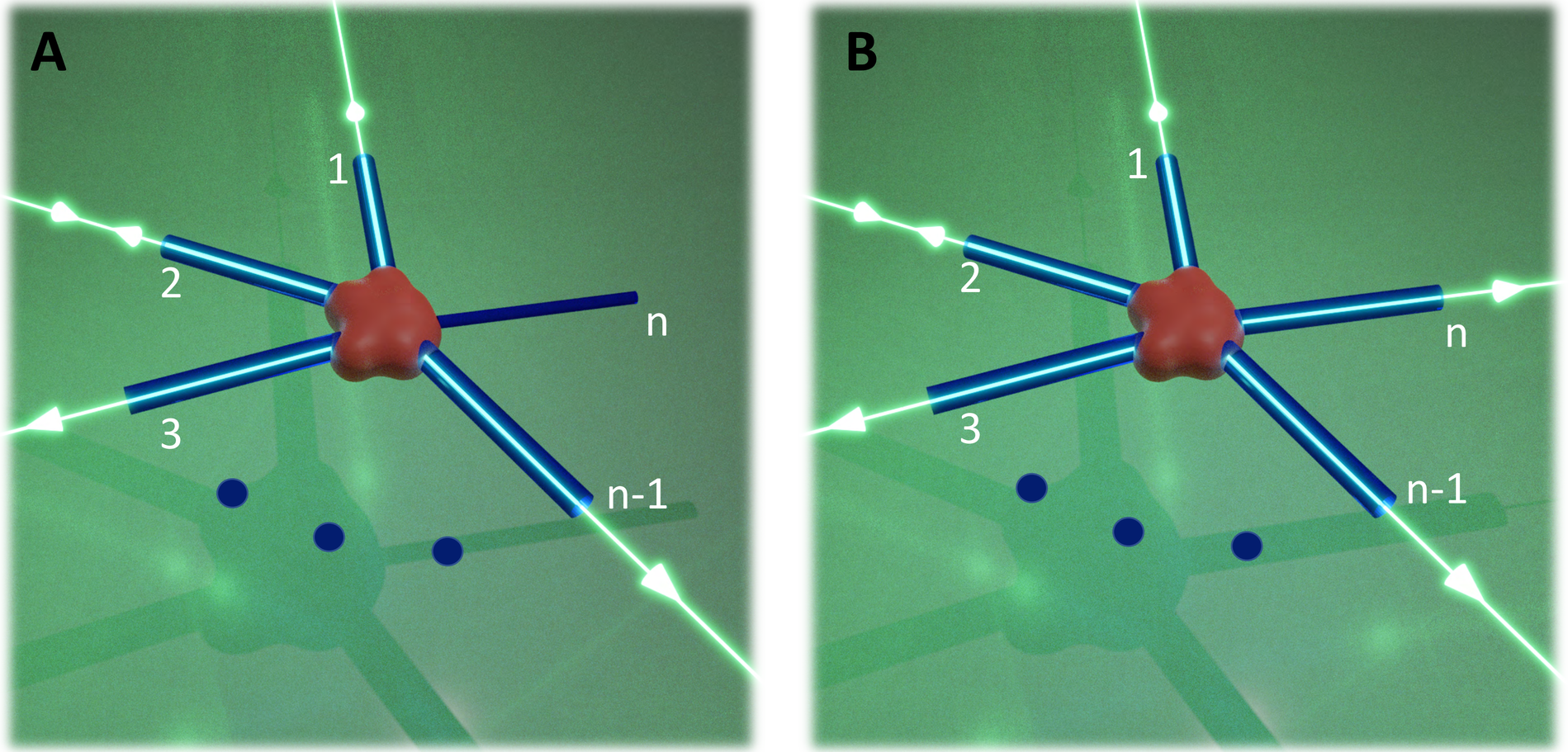

Figure S5: **General setting of a multimoded system with WCA.** An example of a multimoded scattering setting where $n-1$ channels are open while the n-th channel undergoes a transition from **(A)** closed to **(B)** open as an external stimuli enforces variations of the index of refraction which lead to modification of its threshold.

For more details (physical, technical & mathematical) see our paper

Kononchuk *et al.*, *Sci. Adv.* 2021; **7** : eabg8118 4 June 2021

SCIENCE ADVANCES | RESEARCH ARTICLE

APPLIED SCIENCES AND ENGINEERING

Enhanced avionic sensing based on Wigner's cusp anomalies

Rodion Kononchuk[1], Joshua Feinberg[2], Joseph Knee[3], Tsampikos Kottos[1]*

Typical sensors detect small perturbations by measuring their effects on a physical observable, using a linear response principle (LRP). It turns out that once LRP is abandoned, new opportunities emerge. A prominent example is resonant systems operating near *N*th-order exceptional point degeneracies (EPDs) where a small perturbation $\varepsilon \ll 1$ activates an inherent sublinear response $\sim \sqrt[N]{\varepsilon} \gg \varepsilon$ in resonant splitting. Here, we propose an alternative sublinear optomechanical sensing scheme that is rooted in Wigner's cusp anomalies (WCAs), first discussed in the framework of nuclear reactions: a frequency-dependent square-root singularity of the differential scattering cross section around the energy threshold of a newly opened channel, which we use to amplify small perturbations. WCA hypersensitivity can be applied in a variety of sensing applications, besides optomechanical accelerometry discussed in this paper. Our WCA platforms are compact, do not require a judicious arrangement of active elements (unlike EPD platforms), and, if chosen, can be cavity free.